



Highly enhanced thermoelectric and mechanical properties of Bi₂Te₃ hybrid nanocomposite with inclusion of Pt nanoparticles and SWCNTs

Khairul Fadzli Samat^{1,a)} , Yijie Li², Nguyen Van Toan^{2,3}, Mohd Asyadi Azam¹, Takahito Ono^{2,3,a)}

¹Fakulti Kejuruteraan Pembuatan, Universiti Teknikal Malaysia Melaka, 76100 Durian Tunggal, Melaka, Malaysia

²Department of Mechanical Systems Engineering, Tohoku University, Aoba-ku, Sendai 980-8579, Japan

³Micro System Integration Center, Tohoku University, Aoba-ku, Sendai 980-8579, Japan

^{a)}Address all correspondence to these authors. e-mails: khairul.fadzli@utem.edu.my; ono@nme.mech.tohoku.ac.jp

Received: 29 March 2022; accepted: 3 August 2022; published online: 23 August 2022

In this work, an approach of a hybrid inclusion of Pt nanoparticles and single-walled carbon nanotubes (SWCNTs) in a bismuth telluride (Bi₂Te₃) matrix is developed to enhance the thermoelectric and micromechanical properties. The Pt-SWCNTs/Bi₂Te₃ nanocomposite films (up to 0.9 wt% of Pt nanoparticles with 4.8 wt% of SWCNTs) have been synthesized using a three-electrode potentiostatic electrodeposition system. A substantial enhancement of the thermoelectric power factor at 0.6 wt% of the Pt nanoparticles was recorded due to a large increment of Seebeck coefficient. The measured thermal conductivity values indicated 68% of reduction resulted from a large phonon scattering. These improvements result in a remarkable enhancement on overall thermoelectric performance with the figure of merit, *ZT* value reaching 0.99 at room temperature. Meanwhile, in micromechanical analysis, the hardness and Young' modulus values of the nanocomposite increased about 1.5 times and 3.4 times higher than those of a pristine Bi₂Te₃ film, respectively.

Introduction

Thermal energy harvesting process is one of the energy harvesting methods, which is based on the conversion of thermal energy into electrical energy using a thermoelectric generator (TEG) device. In line with recent remarkable developments of Internet of Things (IoT) systems and micro energy-autonomous systems [1–3], the micro-TEG (μ -TEG) devices have become one of the popular types of research to fulfill the demand in micro integrated powering systems such as wearable devices and wireless sensor networks [4]. However, the μ -TEG device based on thermoelectric films usually suffered from low performance of energy conversion especially in room temperature applications. Generally, the thermoelectric films attribute to a relatively lower conversion efficiency in low temperature (< 300 °C) application due to smaller value of absolute temperature and a lesser harvested thermal energy [5]. The efficiency can be calculated by a dimensionless figure of merit, expressed as $ZT = (S^2\sigma/\kappa)T$ which involves the values of Seebeck coefficient (*S*), electrical

conductivity (σ), thermal conductivity (κ), and absolute temperature (*T*) of a thermoelectric material. Even the most commonly used thermoelectric material, a bulk Bi₂Te₃, which already has high *ZT* near room temperature (up to 0.7) [5–8] would have dropped to 0.16 when it is being synthesized in the film condition by electrochemical deposition [9, 10]. The use of electrochemical deposition in the synthesis process is preferred due to cost-effective method, high-efficient technique, and the integration capability in microfabrication process [11, 12].

To improve thermoelectric performance, one needs to increase *ZT* by increasing the power factor ($PF = S^2\sigma$) and reducing the thermal conductivity, simultaneously. This can be achieved by using the synthesis route of nanocomposite process especially in the improvement of Bi₂Te₃. Typically, the composites of thermoelectric material especially with nano inclusion increased the phonon scattering and caused significant reduction of lattice thermal conductivity [13, 14]. The nanofiller inclusion provides selective phonon scattering at the interface

between the nanofiller and bismuth telluride matrix. This scattering mechanism allows the electrons with shorter mean free paths to pass and reduces the effect of electrical resistivity increment [14]. In addition, the inclusion of fillers or layered materials in thermoelectric composite can largely diminish electrical resistivity by reducing the bandgaps and promotes a resistance-free path for the electrons [15, 16]. Generally, the research on the metal nanoparticle inclusion for the thermoelectric nanocomposite material is limited especially through the synthesis method of electrochemical deposition. Recent work by Nguyen et al. shows that the incorporation of Au nanoparticles with 5.0 nm diameter into Bi₂Te₃ through a co-electrodeposition technique significantly increased the Seebeck coefficient but reduced electrical conductivity dramatically [17]. The improvement was mainly caused by potential difference between Au particles and Bi₂Te₃ matrix, and the potential difference acted as energy-dependent barrier. A Cu nanoparticle-Bi₂Te₃ composite formed by plasma sintering exhibits a higher Seebeck coefficient and a lower carrier concentration than those of pure Bi₂Te₃ [18]. All the works of nanocomposites that involve metal nanoparticles including the Ag nanoparticles [17–19] experienced a significant reduction of the thermal conductivity and lead to a high ZT value.

Despite the advantages of metal nanoparticles in contributing of ZT enhancement in nanocomposite study, to date, there has been no definitive evidence that can ensure that metal nanoparticles incorporation improved mechanical properties as well. One of nanomaterials that can highly affect both improvements in thermoelectric and mechanical properties is carbon nanotubes (CNTs) including single-walled CNTs (SWCNTs) and multi-walled CNTs (MWCNTs). While graphene is excellent in enhancing thermoelectric performance, the CNTs play an important role in increasing mechanical properties than the stand-alone graphene inclusion. Recent study shows that the hybrid inclusion of both graphene and CNTs was found capable of increasing mechanical properties while maintaining thermoelectric figures of merit [20]. Over the past decades, CNTs have already been studied on polymer-based composites and steadily benefited for the improvement of both properties [21, 22]. There have been a few studies related to CNTs/Bi₂Te₃ composites in contrast to thermoelectric investigation, and much

less information about the effects of mechanical strengthening [23–25]. The study from An et al. revealed that the CNTs have helped to increase thermoelectric power factor of CNTs/Bi₂Te₃ nanowire composite films by increasing the electron concentration and, on top of that, the composite benefited in elasticity behavior which is suitable for flexible device applications [26].

This work provides a method to synthesis a new electrodeposited film of Bi₂Te₃ nanocomposite with the inclusion of both SWCNTs and Pt nanoparticles. The incorporation of SWCNTs into Bi₂Te₃ was confirmed to have the capability of increasing the Seebeck coefficient; however, it had some uncertainty on improving the electrical conductivity [25, 27]. The same applied to Pt nanoparticles, the latest study on the Pt/Bi₂Te₃ nanocomposite shows that the Seebeck coefficient has significantly increased due to the reduction of electron carrier density in the nanocomposite [28]. In addition, Kang et al. in their study claimed that the existence of Pt nanoparticles in a Sb₂Te₃ matrix had caused the band-bending potential formation and multiplied the Seebeck coefficient [29]. All these studies either utilizing SWCNTs or Pt nanoparticles successfully reduced thermal conductivity through the effective scattering mechanism of phonon. These results motivate this study, in which the association of both SWCNTs and Pt nanoparticles in the Bi₂Te₃ can be expected to enhance the ZT value in overall. Furthermore, with the CNTs involvement in the synthesized nanocomposite in this study, one can predict that there should be some improvement in mechanical strength which will benefit microdevice fabrication. Therefore, this study sets out to develop an electrodeposition method of Pt-SWCNTs/Bi₂Te₃ nanocomposites and objectively assess its thermoelectric and micromechanical properties.

Results and discussion

Composition, morphological, and co-deposition analysis

Table 1 shows the amounts of the Pt nanoparticles and the SWCNTs blended into each electrolyte. Basically, there were four types of the electrolytes (I–IV), in which the contained Pt nanoparticles wt% were varied to synthesize a different composition of the films. In average, there was no significant change in SWCNTs content of the nanocomposite films since the weight percentages

TABLE 1: Pt nanoparticles and SWCNTs concentrations in electrolyte solutions and deposited films.

Electrolyte	Nano-material concentration in electrolyte (g/L)		Deposited films	Nano-material content in deposited film (wt%)	
	Pt nanoparticles	SWCNTs		Pt nanoparticles	SWCNTs
I	0.0	0.0	Bi ₂ Te ₃	0.0	0.0
II	0.05	0.2	Pt-SWCNTs/Bi ₂ Te ₃ -A	0.4 ± 0.1	4.8 ± 0.6
III	0.11	0.2	Pt-SWCNTs/Bi ₂ Te ₃ -B	0.6 ± 0.1	4.8 ± 0.6
IV	0.15	0.2	Pt-SWCNTs/Bi ₂ Te ₃ -C	0.9 ± 0.2	4.8 ± 0.6

of SWCNTs were a constant value in all electrolytes. The successful co-deposited amounts of the SWCNTs in the films were measured at about 4.8 wt%. The initiated lowest fraction of amount of the Pt nanoparticles in the nanocomposite films was 0.4 wt%. The amount of co-deposited Pt could be increased by regularly increasing the Pt nanoparticles concentration in the electrolyte. The thin films with Pt nanoparticles up to 0.9 wt% were prepared prior to its thermoelectric property measurements.

A significant difference in size of the Bi_2Te_3 surface-crystal grain structures can be observed through the SEM images for both pristine and nanocomposite films. The nanocomposite films as shown in Fig. 1(b) generally produced a smaller grain size as compared to that of pure Bi_2Te_3 . A typical growth of plate-like microstructures for pristine Bi_2Te_3 as shown in Fig. 1(a) is quite identical with previous studies of electrodeposited films [30–32]. Meanwhile, the magnified SEM images of Fig. 1(a, b) clearly

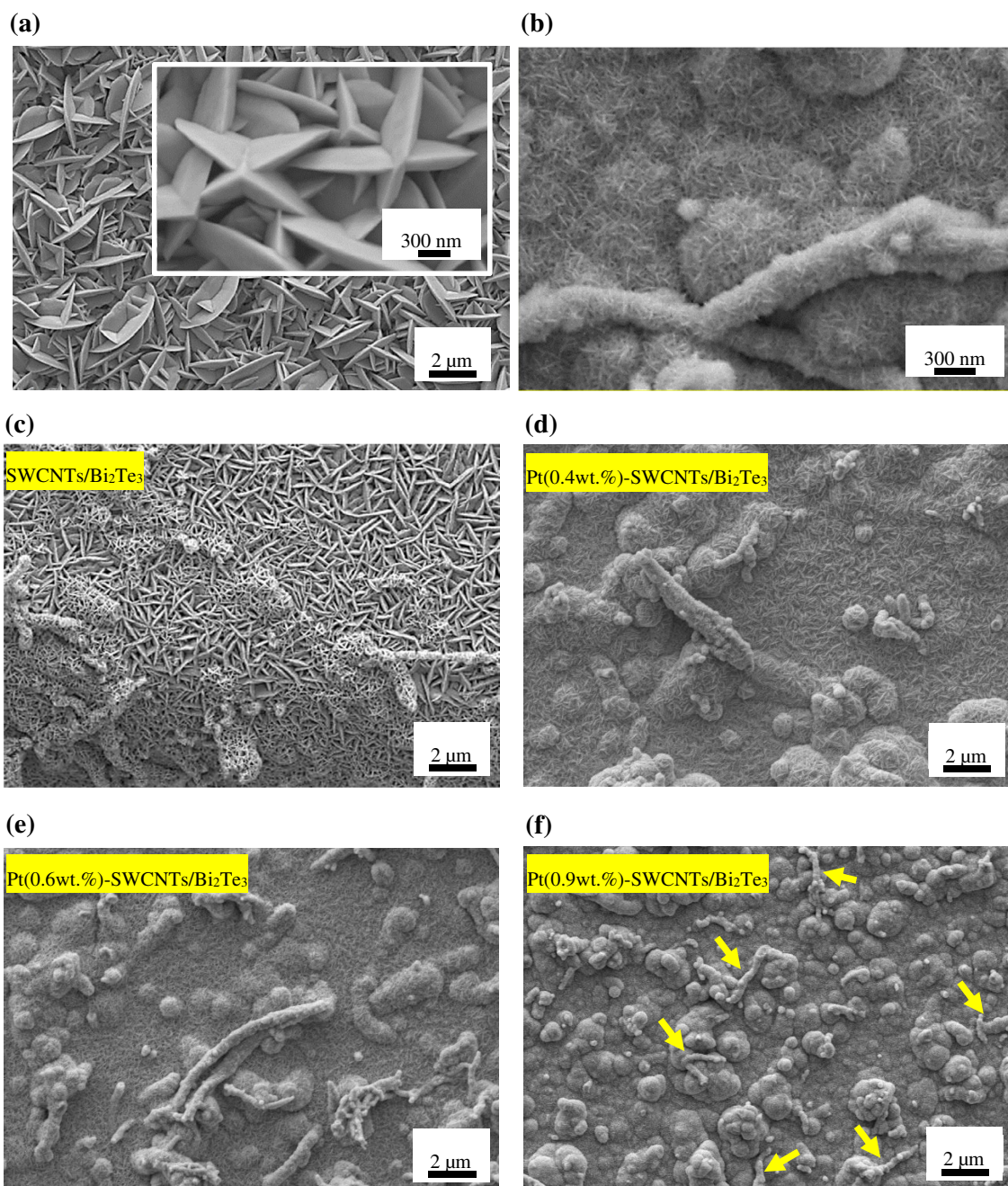


Figure 1: SEM images of the electrodeposited films surface. (a) The pristine Bi_2Te_3 . The inset demonstrates magnified SEM image of the pristine Bi_2Te_3 . (b) Magnified SEM image of the Pt(0.9 wt%)-SWCNTs/ Bi_2Te_3 . (c) SWCNTs/ Bi_2Te_3 . (d–f) Pt-SWCNTs/ Bi_2Te_3 with different Pt wt%. Arrows in the image (f) indicated the dispersed SWCNTs incorporated on the Pt-SWCNTs/ Bi_2Te_3 surface and some of them partly/fully blended in the Bi_2Te_3 matrix.

show the different size of Bi_2Te_3 surface-crystals structures on the nanocomposite film while maintaining the plate-like shape. The inclusion of SWCNTs only in the Bi_2Te_3 matrix promotes reduction of Bi_2Te_3 surface-crystals structure sizes and even further reducing the size with hybrid inclusion of Pt nanoparticles is shown in Fig. 1(c–f). A slow growth of Bi_2Te_3 during the electrochemical deposition process of the nanocomposite might be one of the possible reasons why the grain size was significantly smaller as compared to that of the pure Bi_2Te_3 . Both the nanomaterials need a wrap of the polymer to be suspended and dispersed in the electrolyte. The existence of the polymer in the electrolyte acted as an insulator layer and was partially hindering electron transfer during the reduction of bismuth and telluride ions.

Figure 1(c–f) shows SWCNTs visibly co-deposited onto the film surface and disoriented in random directions. Since the commercialized SWCNTs can be up to 10 μm in length [27], some of the observed SWCNTs were partly incorporated under the crystalline Bi_2Te_3 . The growth of Bi_2Te_3 did not only establish on its overlapped growth but the electrocrystallization also occurred on the surface of the SWCNTs as shown in Fig. 1(b). This could happen if the SWCNTs were partly/fully free from the polymeric wrap during the incorporation process and provided a conductive surface for the nucleation of Bi_2Te_3 . All of these can be explained by understanding the possible mechanisms for the nanomaterials to be co-deposited. One of the conceivable mechanisms might follow the Guglielmi's model where the nanomaterials are proposed to be surrounded by adsorbed cations in electrolyte [33, 34]. The adsorbed ions generated a positive net charged on the Pt nanoparticles and SWCNTs and initiated attraction force in the diffusion layer. The attraction force in the diffusion layer made the nanomaterials capable to temporarily attach on the electrode surface. In the meantime, continuous growth of Bi_2Te_3 near the attached nanomaterials eventually enables the trapping of nanomaterials [30]. The Pt nanoparticles and SWCNTs move toward the electrode depend not only on the diffusion (based on different concentration in electrolyte) but also on the effect of hydrodynamic [35, 36]. As discussed in this study, the electro-steric stabilization may provide a certain degree of positive charges surrounding the Pt nanoparticles and SWCNTs. Therefore, the electromigration might be considered as another factor to aid the particles transportation toward the electrode.

Figure 2 shows the XRD spectrums for the electrodeposited Pt-SWCNTs/ Bi_2Te_3 nanocomposite and pristine Bi_2Te_3 films. The XRD analysis was conducted on the nanocomposite samples with the maximum and minimum Pt wt%. The sample of the pure Bi_2Te_3 film exhibited (015), (1010), and (110) diffraction peaks. The same peaks were detected on the nanocomposite samples with an additional diffraction peak of (0210). All the peaks were confirmed and represented as typical Bi_2Te_3 orientation similar to the previous electrodeposited pure

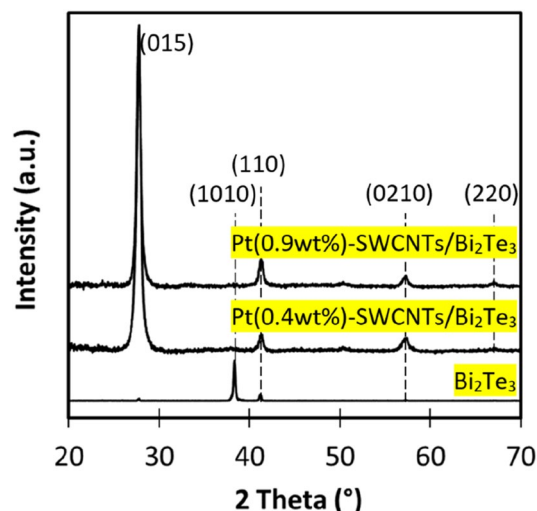


Figure 2: XRD data for pure Bi_2Te_3 and Pt-SWCNTs/ Bi_2Te_3 at 0.4 wt% and 0.9 wt% of Pt nanoparticles deposited.

Bi_2Te_3 [37–39]. All synthesized samples were characterized as polycrystalline structure oriented with different dominance of diffraction peak. Normally, the (1010) orientation was a quite typical dominance orientation for the electrodeposition using negative potential. However, the effect of Pt particles and SWCNTs inclusion in Bi_2Te_3 matrix made the (015) orientation to become significantly dominant and improved the crystallinity of the (110) and (0210) orientations. The existence of strong (015) structure orientation for the nanocomposite films characterized the film's surface to be quite rough with low density [39]. A weak (220) orientation indicated the Pt diffraction peak as compared to the face-centered cubic lattice of Pt [40, 41]; however, the peak was only visible at 0.9 wt% of Pt.

The high-resolution transmission electron microscopy (HRTEM) observation was conducted to analyze the microstructure of the Pt-SWCNTs/ Bi_2Te_3 nanocomposite which consisted of 0.6 wt% Pt nanoparticles. Figure 3(a) shows several black spots area indicating Pt nanoparticles. The average diameter of deposited Pt nanoparticles was about 8.0 nm, near to the value of dispersed Pt nanoparticles in the electrolyte. Figure 3(b) depicts the selected area electron diffraction (SAED) pattern that represents as illuminated rings from diffraction of incident beam, indicating microstructures with randomly oriented small grains. The lattice fringes of the Pt-SWCNTs/ Bi_2Te_3 nanocomposite show lattice defects due to the lattice distortions, as displayed in Fig. 3(c). The inclusion of both SWCNTs and Pt nanoparticles promotes the formation of extrinsic stacking faults as observed at D5 and D6 locations. Other defects such as dislocation core can also be identified at D1–D4 locations. Further analysis on the grain size was performed by utilizing the XRD data through the XRD line broadening analysis. The integral breadth was used to estimate

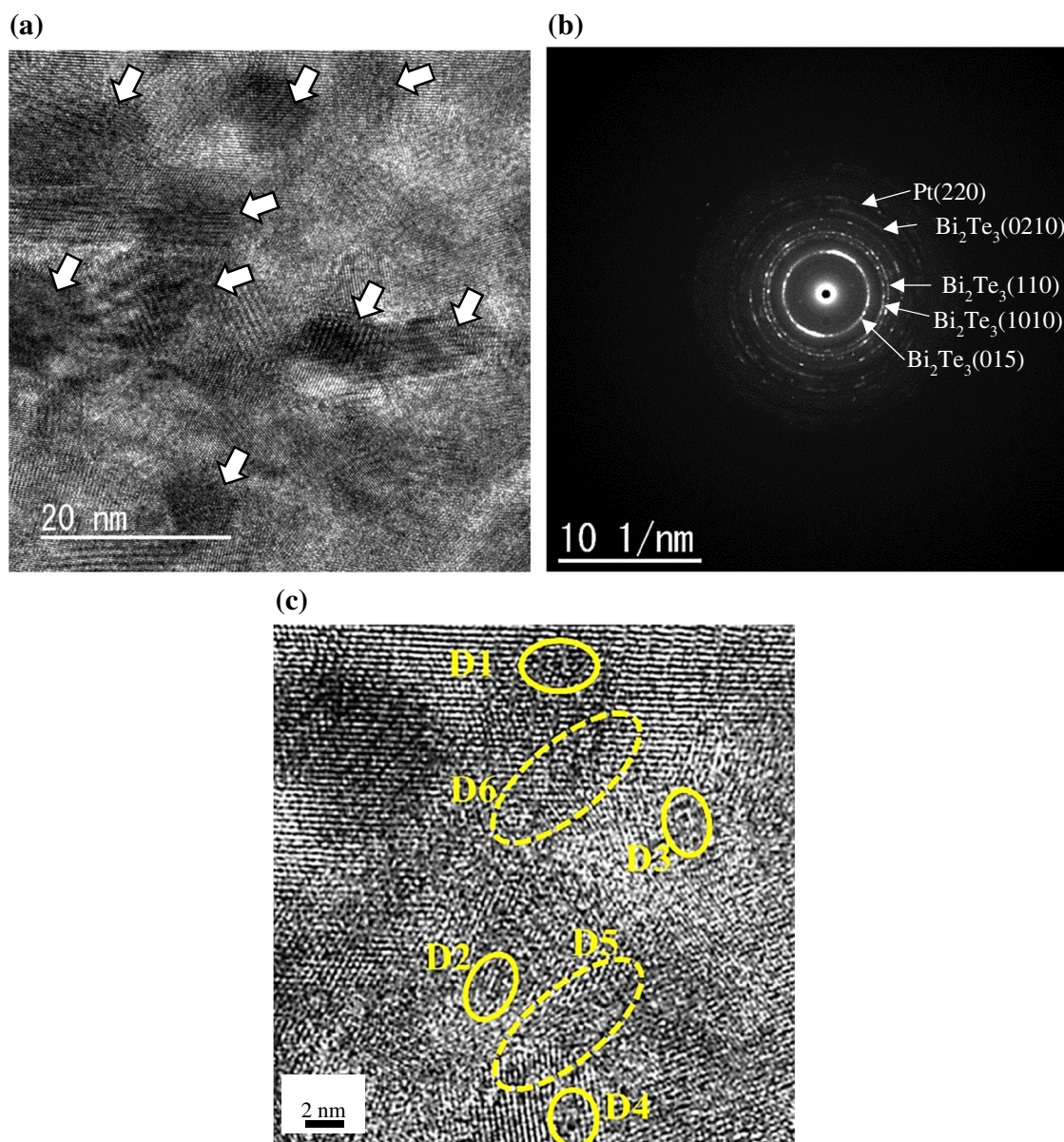


Figure 3: TEM images of the cross-section area of electrodeposited Pt-SWCNTs/Bi₂Te₃ nanocomposite. (a) High resolution of TEM image showing Pt particles (black spots pointed by arrows). (b) Selected area electron diffraction (SAED) pattern. (c) Lattice defects by referring to dislocation cores (D1–D4) and stacking faults (D5 and D6).

the line broadening, and the calculation of the average grain size was computed by Scherrer equation. The average grain size of pristine Bi₂Te₃ was estimated to be about 32 ± 4 nm and the grain size of for the nanocomposite was significantly reduced to 11 ± 3 nm for the lowest Pt nanoparticles content, as listed in Table 2.

Evaluation on thermoelectric power factor

The incorporation of SWCNTs was expected to increase the electrical conductivity based on the result of the SWCNTs/Bi₂Te₃ synthesized in this study as listed in Table 3. The SWCNTs/

Bi₂Te₃ nanocomposite has been synthesized as the same method of the Pt-SWCNTs/Bi₂Te₃ nanocomposite by excluding the mixture of Pt nanoparticles. However, the effect of SWCNTs on enhancing an electrical transportation has been suppressed when the Pt nanoparticles was simultaneously incorporated in the Bi₂Te₃ film. The electrical conductivity of the nanocomposite reduced regularly as the Pt content increased as shown in Fig. 4(a). The largest drop of the electrical conductivity was at 0.9 wt% of Pt nanoparticles. The reduced electrical conductivity affected by a lower carrier concentration as shown in Table 3 characterizes a typical semiconductor composite materials

behavior [5, 42]. This phenomenon of lower carrier concentration of the Bi₂Te₃-based nanocomposite also occurred on the previous study of electrodeposited Pt/Bi₂Te₃ film [28]. The study proved that the presence of the Pt nanoparticles in the Bi₂Te₃ matrix decreased the carrier concentration as compared to the pristine Bi₂Te₃ film. A decreased n-type carrier concentration of the Pt-SWCNTs/Bi₂Te₃ nanocomposite signified an increase of holes carrier concentration. The Pt nanoparticles inclusion possibly developed a significant number of acceptors, which functions as a hole due to its positive potential [43].

A study from Ko et al. proved that the Pt nanoparticles inclusion in the Sb₂Te₃ matrix is capable to increase the holes carrier concentration to up to 2.5 times than a pristine Sb₂Te₃. Their study proposed that the incorporation of Pt nanoparticles enlarged the gap between Fermi energy level and the valence

band of Sb₂Te₃, thus noticeably increased the number of holes [29]. This might happen to Bi₂Te₃ as well, which eventually reduced the total fraction of the carrier concentration and reduced fermi energy level of Bi₂Te₃ matrix. Similarly, it happened to Cu particles incorporation into Bi₂Te₃ as reported in reference [18], in which the carrier concentration has reduced significantly to more than half as compared to pure Bi₂Te₃ at only 0.13 wt% Cu content. Despite the effect from Pt nanoparticles, the existence of SWCNTs in Pt-SWCNTs/Bi₂Te₃ nanocomposites looks like it further enhanced the high Seebeck coefficient for Bi₂Te₃. The possibility for SWCNTs to increase Seebeck coefficient cannot be denied since it had been proven in previous studies [25, 27]. Both studies were in a good agreement to state that an optimized content of SWCNTs in the Bi₂Te₃ matrix can noticeably increase the Seebeck coefficient.

TABLE 2: Summary of average grain size and microstrain on pristine Bi₂Te₃ and Pt/Bi₂Te₃ nanocomposite films at 2θ = 27.7°, 41.3°, and 57.3°.

Electrodeposited films	Co-deposited Pt nanoparticles (wt%)	Co-deposited SWCNTs (wt%)	Integral Breadth, β at 2θ=27.7, [rad]	Average grain size [nm]	Average microstrain (10 ⁻³)
Bi ₂ Te ₃	0.0	0.0	0.6 × 10 ⁻²	32	4.3
Pt-SWCNTs/Bi ₂ Te ₃ -A	0.4 ± 0.1	4.8 ± 0.6	1.1 × 10 ⁻²	12	9.8
Pt-SWCNTs/Bi ₂ Te ₃ -C	0.9 ± 0.2	4.8 ± 0.6	1.2 × 10 ⁻²	11	10.7

TABLE 3: Summary of electrical properties of pristine Bi₂Te₃ films, SWCNTs/Bi₂Te₃, and Pt-SWCNTs/Bi₂Te₃ nanocomposite films studied in this work and Pt/Bi₂Te₃ nanocomposite film from author's previous work [28].

Type of films	Pt (wt%)	SWCNTs (wt%)	Seebeck coefficient [μV K ⁻¹]	Electrical conductivity [S cm ⁻¹]	Power factor [μW m ⁻¹ K ⁻²]	Carrier concentration, n (× 10 ¹⁷) [cm ⁻³]
Bi ₂ Te ₃	–	–	– 115	620	820	4.5 ± 1.0
Pt/Bi ₂ Te ₃ [23]	1.9	–	– 184	528	528	1.9 ± 0.1
SWCNTs/Bi ₂ Te ₃	–	4.4	– 51	1487	381	15.1 ± 2.0
Pt-SWCNTs/Bi ₂ Te ₃ -C	0.9	4.8	– 226	290	1477	0.8 ± 0.1

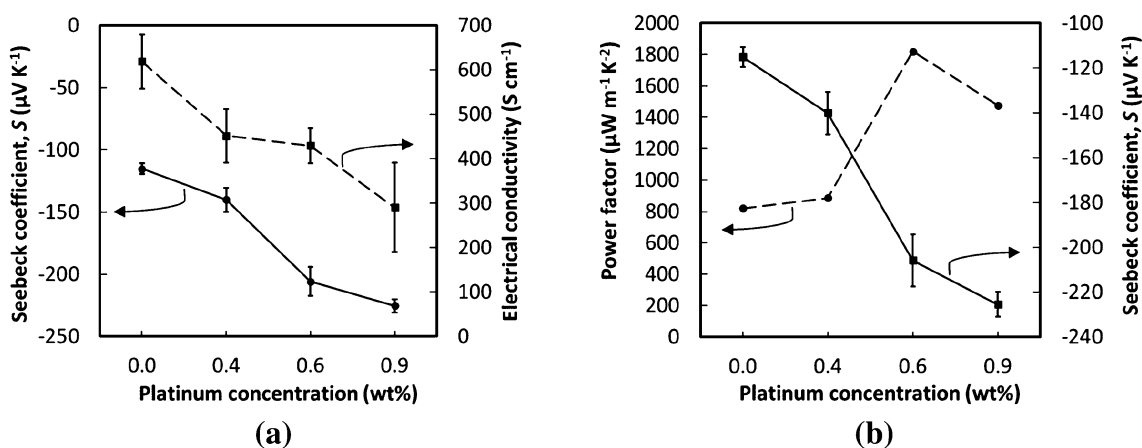


Figure 4: Deposited Pt nanoparticle concentration dependence of (a) Seebeck coefficient and electrical conductivity. (b) Power factor and Seebeck coefficient. All nanocomposite films had 4.8 wt% of SWCNTs.

In contrast with the performance of the electrical conductivity, the Seebeck coefficient of Pt-SWCNTs/Bi₂Te₃ was significantly improved as Pt nanoparticles content increase. The Seebeck coefficient can be reduced by reducing the carrier concentration as reported from previous findings regarding metal particles inclusion in Bi₂Te₃ [18, 28]. As referred to the comparison of carrier concentrations with a pristine Bi₂Te₃ film and other nanocomposite films shown in Table 3, it had a reasonable trend that the lower carrier concentration contributes to higher Seebeck coefficient. The contradict effect was identical with the Seebeck coefficient, *S* formula based on basic theory of free electrons [44],

$$S = (8\pi^2 k_B^2 / 3eh^2) m^* T (\pi / 3n)^{2/3}, \quad (1)$$

where *k_B*, *h*, *e*, *n*, and *m^{*}* are Boltzmann's constant, Planck's constant, electronic charge, carrier concentration, and effective mass of the carrier. The expression strongly proposed that a thermoelectric material with lower carrier density has a higher Seebeck coefficient value. Figure 4(b) shows the calculated thermoelectric power factor increased for the Pt-SWCNTs/Bi₂Te₃ nanocomposite as compared to the pure Bi₂Te₃ due to high contribution of Seebeck coefficient value. The optimum value of power factor was recorded at 0.6 wt% of Pt nanoparticles even though the maximum Seebeck coefficient was recorded at maximum content of Pt nanoparticles due to significant reduction electrical conductivity. Table 3 also shows that the calculated power factor was mainly affected by the value of Seebeck coefficient based on the comparison of Pt/Bi₂Te₃, SWCNTs/Bi₂Te₃, and Pt-SWCNTs/Bi₂Te₃ nanocomposite films.

Evaluation on thermal conductivity and ZT

Figure 5(a) shows the temperature different dependence of the applied frequency for every synthesized film, and the calculated value of thermal conductivity is shown in Fig. 5(b). As the Pt nanoparticles content increased, the thermal conductivity value dropped at lower value than one-third of the value of pure Bi₂Te₃. Thermal conductivity of semiconductor materials is mainly determined by lattice thermal contribution. In general, lattice vibration greatly influences the phonon mean free path according to the kinetic and the Boltzmann transport equation theories [45–47]. In other words, low thermal conductivity recorded for the nanocomposite film might be based on a reduction of phonon mean free path. There are three mechanisms of scattering process that can affect the phonon free path as explained by Matthiessen's phonon free path formulation [45]: the effect of boundary, impurity, and phonon–phonon scattering processes. The combination effect of impurity scattering process provided by Pt nanoparticles and SWCNTs inclusions additionally enhanced the mid to long-wavelength phonons scattering mechanism [48].

It is worth to mention that the long-wavelength phonon is dominant in thermal transportation at room temperature condition according to Wien's displacement law for phonons states [47]. Therefore, every effect that is capable of increasing scattering mechanism of the long-wavelength phonon can largely influence the reduction of thermal conductivity, including the effect of the distance between the included Pt nanoparticles. Based on TEM images, the shortest distance between the Pt nanoparticles can be lower than 5.0 nm. The

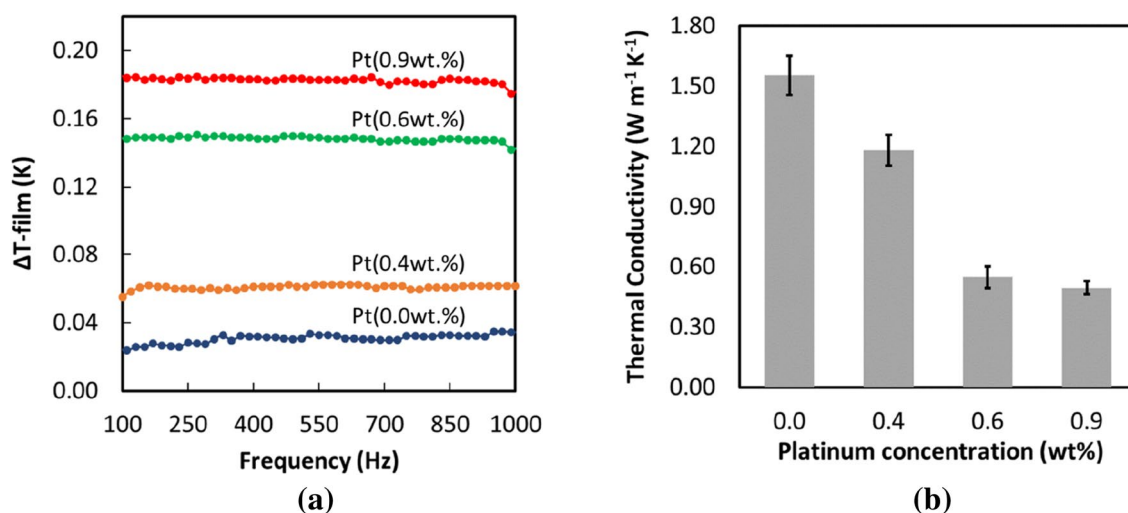


Figure 5: Thermal conductivity results obtained from the differential 3ω method measurement system. (a) Effective temperature difference for the synthesized films as a function of frequency. (b) Calculated thermal conductivity for a pure Bi₂Te₃ and different Pt nanoparticles content in the Pt-SWCNTs/Bi₂Te₃.

nanometer-order distance between the particles increased the phonon scattering as it is closed to the value of Bi_2Te_3 mean free path [48]. Furthermore, the existence of Pt nanoparticles in the nanocomposite acted as localized barriers which can effectively scatter the mid to long-wavelength phonon as proven in the previous study of $\text{Pt}/\text{Bi}_2\text{Te}_{2.7}\text{Se}_{0.3}$ nanocomposite film [49].

The hybrid effect contributed by Pt nanoparticles and SWCNTs inclusions can be verified by comparing the $\text{Pt}/\text{Bi}_2\text{Te}_3$ and the $\text{Pt-SWCNTs}/\text{Bi}_2\text{Te}_3$ nanocomposites. The existence of 1.9 wt% of the Pt nanoparticles only in the electrodeposited Bi_2Te_3 film reduced the thermal conductivity to $0.87 \text{ W m}^{-1} \text{ K}^{-1}$ [28]. However, by coexisting inclusion with SWCNTs, the value largely dropped to $0.5 \text{ W m}^{-1} \text{ K}^{-1}$ at even half of the Pt content (0.9 wt%) as depicted in Fig. 5(b). From these results, it is confirmed that the association with SWCNTs exaggerated the reduction of thermal conductivity. The boundary between the Bi_2Te_3 and the nanomaterials might deliver another mechanism to scatter the long-wavelength phonon. The incorporated SWCNTs in Bi_2Te_3 most probably developed the incoherent interface between Bi_2Te_3 and SWCNTs, which intensified the phonon scattering through the boundary, as reported by Ahmad and Wan [27]. Moreover, a smaller grain size attributed by the $\text{Pt-SWCNTs}/\text{Bi}_2\text{Te}_3$ nanocomposite as compared to pristine Bi_2Te_3 also contributed in scattering the phonon. Smaller grain size means higher density of grain boundaries, which might enhance the boundary scattering effect. The grain size effect on the thermal conductivity in this study seems to be consistent with previous studies that specifically reported on pure Bi_2Te_3 [50, 51]. Those studies came to an agreement where the phonon will be effectively scattered with a finer grain size due to grain boundaries scattering mechanism.

The densities of crystal structural defects including the point defect and stacking fault in a nanocomposite matrix are normally quite higher than that of the pristine one as reported in the previous studies [26, 28, 52]. The defect density may be worst in the condition of smaller grain growth as in the $\text{Pt-SWCNTs}/\text{Bi}_2\text{Te}_3$ nanocomposite due to high number of point defects. As proved by Gleiter, the point defects tend to exist in the grain boundary which can contribute to the increment of the defect density [53]. The existence of crystal defects effectively scattered the short-wavelength phonon in the nanocomposite because of the scattering mechanism of mass-difference and local strain fields generated [49, 54]. As a result of the poor thermal conductivity exhibited by the nanocomposite films, the calculated figure of merit, ZT reached to 0.99, which is a more than five times increment than that of the pristine Bi_2Te_3 film. The significant high ZT values were clearly observed at Pt content 0.6 and 0.9 wt% due to a substantially low thermal conductivity (less than $0.6 \text{ W m}^{-1} \text{ K}^{-1}$) and high power factor, as shown in Fig. 6.

Evaluation on micromechanical properties of $\text{Pt-SWCNTs}/\text{Bi}_2\text{Te}_3$

Figure 7(a) shows typical curves of indentation depth corresponding to measured load by the ultramicro-indentation device on the synthesized samples consisting of a pristine Bi_2Te_3 and two different compositions of the $\text{Pt-SWCNTs}/\text{Bi}_2\text{Te}_3$ nanocomposite films. One of the nanocomposite samples, the $\text{Pt-SWCNTs}/\text{Bi}_2\text{Te}_3$ -I, had similar composition of Pt nanoparticles and SWCNTs with the $\text{Pt-SWCNTs}/\text{Bi}_2\text{Te}_3$ -C as listed in Table 1. On the other hand, the $\text{Pt-SWCNTs}/\text{Bi}_2\text{Te}_3$ -II had 37% higher amount of SWCNTs in the matrix and same content of Pt nanoparticles. The penetration depth ranged within $0.4\text{--}0.8 \mu\text{m}$ and was maintained to be less than 10% of the sample thickness to avoid any possibility of the substrate

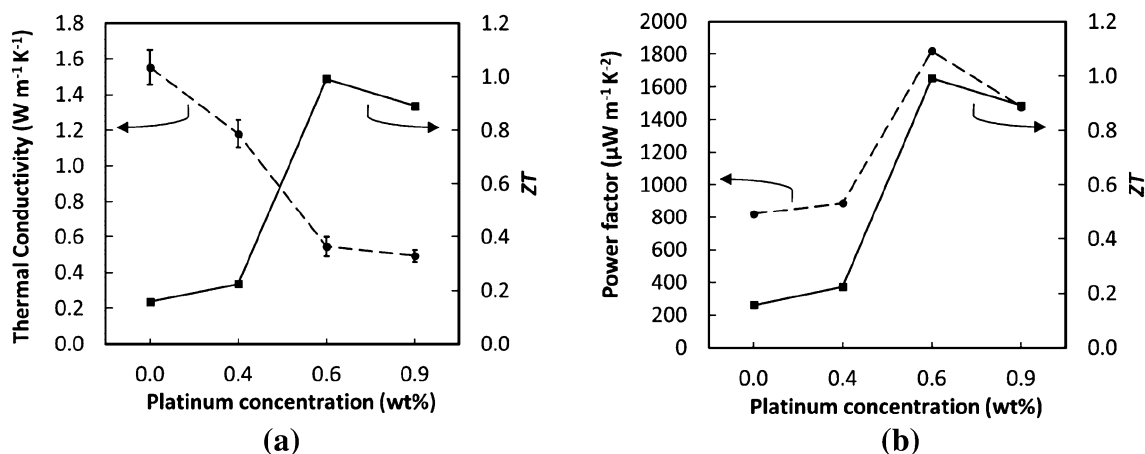


Figure 6: Deposited Pt nanoparticle concentration dependence of; (a) Thermal conductivity and thermoelectric figure of merit, ZT . (b) Power factor and thermoelectric figure of merit, ZT at room temperature. All nanocomposite films had 4.8 wt% of SWCNTs.

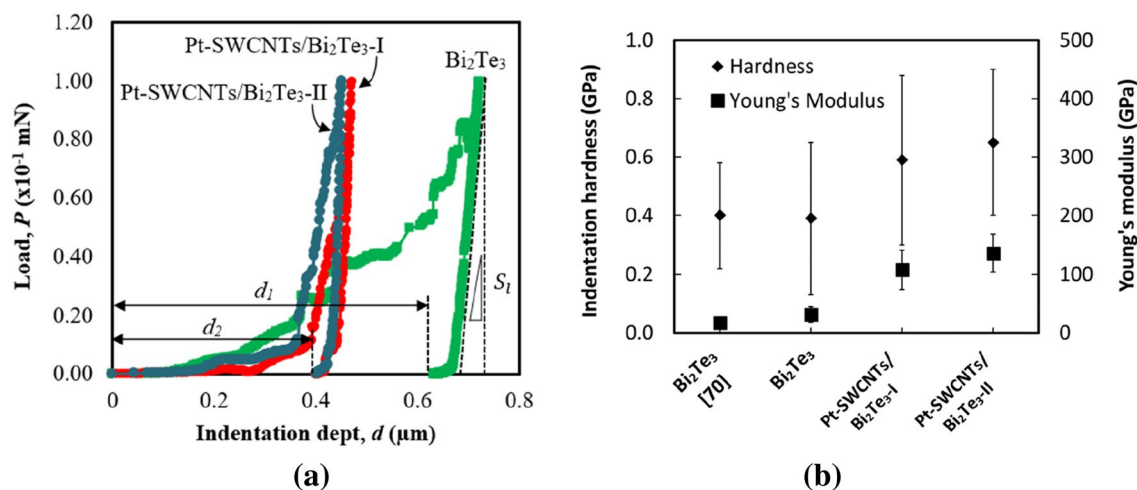


Figure 7: (a) Indentation depth dependence of force for both pristine Bi_2Te_3 and Pt-SWCNTs/ Bi_2Te_3 nanocomposite films. (b) Measured hardness and estimated Young's modulus of Bi_2Te_3 and Pt-SWCNTs Bi_2Te_3 films.

influence. The observed depth–load curve based on the existence of elastic and plastic deformations of samples during the indentation process encompasses the loading and unloading stages. Generally, the load values increased as the indenter penetrated the sample surface and exponentially increased depending on the hardness of sample. The hardness measurement provided a degree of validation by producing consistent hardness value of pure Bi_2Te_3 film with the previous work of an electrodeposited Bi_2Te_3 film [55] as shown in Fig. 7(b).

In overall, Pt-SWCNTs/ Bi_2Te_3 nanocomposite films took less indentation depth as compared to pure sample of Bi_2Te_3 ($d_2 < d_1$). The lower distance of penetration shows that the nanocomposite material attributed to higher hardness properties, which provided more resistance for the material to deform. Figure 7(b) presents the measured hardness of the Pt-SWCNTs/ Bi_2Te_3 -I nanocomposites increases to 0.67 GPa, which is 72% increment as compared to the pristine sample. The figure also shows the estimated Young's modulus of the Pt-SWCNTs/ Bi_2Te_3 -I nanocomposite significantly increased at about 3.4 times higher than that of the pristine sample. In reference to the grain size reduction in the nanocomposite, grain-boundary strengthening (also known as Hall–Petch strengthening) might be one of the reasons that hindered plastic deformation through the dislocation mechanism.

Higher hardness and higher Young's modulus recorded for the nanocomposite attribute to the decorated SWCNTs that acted as reinforced materials to hinder the localized plastic deformation. The Van der Waals force developed at the interface of the Bi_2Te_3 and SWCNTs leads to steady interfacial bonding which able to transfer the load from Bi_2Te_3 matrix to SWCNTs additive [56]. With superior Young's modulus of SWCNTs (~ 1000 GPa) [57], the deformation initiation will be efficiently suppressed at any load transferred. In general, the

covalent functionalized CNTs provide better interfacial bonding in nanocomposite phase due to the involvement of strong covalent bonding. Although the capability to load transfer is quite limited due to the non-covalent (polymer wrapping) functionalization of SWCNTs prepared in this study, it still has a certain degree of effect for load transfer capability [58, 59]. In addition, due to possible existence of electrostatic interaction between the SWCNTs additive and the Bi_2Te_3 matrix, the combination effect with Van der Waals force further enhanced the interfacial load transfer ability [60]. The main role of SWCNTs in the enhancement was verified by the result of Pt-SWCNTs/ Bi_2Te_3 -II. About 10% and 30% improvement of hardness and Young's modulus, respectively, exhibited by the Pt-SWCNTs/ Bi_2Te_3 -II is compared to the Pt-SWCNTs/ Bi_2Te_3 -I nanocomposite. By obtaining both improvements, it clearly can be seen that, the increase of SWCNTs amount would increase the mechanical strength of the Bi_2Te_3 film.

Conclusions

This study presented a novel method to incorporate two nanomaterials: Pt nanoparticle and SWCNTs, into a Bi_2Te_3 matrix. The nanocomposite films were prepared with different Pt contents but maintained at same amount of SWCNTs (4.8 wt%). The existence of Pt nanoparticles and SWCNTs in the Pt-SWCNTs/ Bi_2Te_3 nanocomposite film changed both the grain size and the carrier concentration significantly, as compared to the pure Bi_2Te_3 film. The electron density for the nanocomposite decreased and reduced the electrical conductivity as the Pt content increases. The reduced electron concentration benefited the Seebeck coefficient of the nanocomposite, where the value was significantly increased to almost twice than that of pure Bi_2Te_3 film. This

resulted in the increased thermoelectric power factor to $1820 \mu\text{Wm}^{-1} \text{K}^{-2}$ which was more than two-time increment at an optimized 0.6 wt% Pt nanoparticles content. The impurity scattering mechanism caused by the Pt nanoparticles and SWCNTs in the Bi_2Te_3 phase was one of the factors that effectively scattered the mid to long-wavelength phonons. As a result, the thermal conductivity attributed by the Pt-SWCNTs/ Bi_2Te_3 nanocomposite films largely dropped to $0.5 \text{Wm}^{-1} \text{K}^{-1}$. High Seebeck coefficient and low value of thermal conductivity for the nanocomposite films lead to a notable increase in ZT up to ~ 1.0 at room temperature. Despite the excellent thermoelectric properties, the mechanical strength in hardness and elastic modulus also increased as compared to the pristine film. High reinforcing effect caused by SWCNTs incorporation in the nanocomposite could be the main factor in enhancing the mechanical properties.

Materials and methods

Nanocomposite synthesis process

Both the pristine Bi_2Te_3 and Pt-SWCNTs/ Bi_2Te_3 nanocomposite films were synthesized by a potentiostatic electrochemical deposition system with a three-electrode cell at room temperature. The electrochemical cell encompassed Pt strip as a counter electrode, silver/silver chloride (Ag/AgCl) as a reference electrode, and a chromium–gold (Cr/Au) seed layer on a glass substrate as a working electrode. The Cr/Au seed layer was formed by a magnetron sputtering system. All electrolyte solutions consisted of 3.2 mM Bi^{3+} and 7.2 mM HTeO^{2+} ions in 1.0 M nitric acid (HNO_3). The electrolytes used for the deposition of nanocomposite films were prepared with a mixture of 2.0 nm-diameter Pt nanoparticles (0.03–0.10 g/L) and SWCNTs (0.2 g/L). The commercially prepared Pt nanoparticles with a diameter of 2.0 nm were in a liquid form blended in a polyvinylpyrrolidone (PVP) solution, where it can be expected that the Pt nanoparticles were covered by the polymeric molecules to enhance the affinity to aqueous solutions. Same concept also applicable to SWCNTs, in which the surface must be coated by polymeric molecules to enhance the solubility in the aqueous electrolyte.

Typically, CNTs have very low hydrophilicity and stability in aqueous solutions, which can easily lead to aggregation issue. This aggregation is mainly caused by the hydrophobicity and strong Van der Waals interaction among the CNTs [61]. Therefore, the SWCNTs need to be modified to provide hydrophilic surface property. In this study, an easy method to modify the SWCNTs surface had been carried out through the non-covalent modification, where the surface was wrapped by a cationic polymer, poly(diallyldimethylammonium chloride) (PDDA). Unlike covalent modification which uses surfactant molecules, the non-covalent method does not involve any chemical reaction and carboxyl groups introduction on the SWCNTs surface that might cause a certain degree of graphitic structure damage [62–64]. It

is important to reduce the possibility of CNTs surface damage at the beginning of preparation to avoid a change of intrinsic properties of CNTs, such as electrical conductivity and mechanical toughness [65]. The surface of the CNTs was coated by PDDA using the non-covalent bonding through the mixing, stirring, and sonication processes [66]. The sonication also functions to dissolve the aggregated CNTs while in powder condition. At the end of the sonication step, the SWCNTs were suspended and dispersed in the PDDA solution due to the polymer wrapping effect that is also known as the steric and depletion stabilization [61, 67, 68]. Then, the solution underwent filtration process along with distilled water to remove the excessive PDDA.

The mixing process of polymeric coated of Pt nanoparticles and SWCNTs in the prepared electrolyte solution involved magnetic stirring with constant N_2 purging. Beforehand, the electrolyte went through another two hours of sonication to further stabilize those nanomaterials. Additional functionalization might happen for both the Pt nanoparticles and the SWCNTs due to H^+ (from acidic electrolyte) adsorption on its surface and provided electro-steric stabilization [62, 69]. The electro-co-deposition was performed in a potentiostatic periodic-reverse pulses deposition at room temperature. Meanwhile, the duty cycle ($T_{\text{on}}/(T_{\text{on}} + T_{\text{off}})$) was controlled at 33% for all depositions with rapid co-deposition occurred during 100 ms of T_{on} at applied potential -90mV , E_{on} . The electrolyte was magnetically stirred at 250 rpm throughout the deposition process to preserve a uniform concentration of the Pt nanoparticles and the SWCNTs. The N_2 purging was also applied during the process to reduce possible incorporation of oxygen. For a pulse electro-deposition method, deposition was carried out to serve better control on the composition and microstructure, which reduces porosity issue and enhances the film structure reliability [70, 71]. With consistent deposition time, the film thickness was maintained at approximately $1 \mu\text{m}$ (measured by scanning electron microscopy image of cross-sectional sample).

Measurements and analyses

The morphological study to analyze the crystallite formation of synthesized films was performed by using scanning electron microscopy (SEM) and its crystal structures were characterized. The energy-dispersive X-ray spectroscopy (EDX) was used to measure the elemental composition of the deposited films. The crystal structures were characterized by X-ray diffraction (XRD) spectrum with $\text{Cu}(\text{K}\alpha)$ radiation ($\lambda = 0.15418 \text{nm}$). The crystallographic orientation and lattice defects were confirmed by high-resolution images of TEM (HRTEM), selected area electron diffraction (SAED), and weak-beam dark field (WBDF). The electrical conductivity was recorded by measuring the sheet resistivity of all samples through four-probe resistivity measurement. A Seebeck measurement system had been used to measure

the generated voltage and temperature difference by a steady-state method. All samples were transferred into molded epoxy as an insulator layer. Both measurements of electrical conductivity and Seebeck coefficient had been conducted at room temperature and systematically compared with previous works of electrodeposited Bi_2Te_3 films [28, 72].

The carrier concentration of the samples was evaluated by a four-probe Hall voltage measurement system, and the related calculation was referred to the standard test method of ASTM International F76-86 [73]. This study used a differential 3ω method to evaluate the thermal conductivity of all samples. Two types of specimens need to be prepared; one of them is a specimen with the deposited film (called as sample specimen) and the other is without any deposited film (called as reference specimen). Both types of specimens were required for the fabrication of a resistive micro heater on the surface of the sample and the reference. Details of the microfabrication parameter and process can be referred to the previous work [28]. The fabricated micro heater on both specimens also functioned as a thermometer to record the temperature variation of the deposited film through the change of the first ($V_{1\omega}$) and third ($V_{3\omega}$) harmonic voltages. The effective temperature differences across the deposited film (ΔT_f) on the sample specimen and its thermal conductivity (κ) were calculated by following equations [74],

$$\Delta T_f = \Delta T_s - (P_s/P_r)\Delta T_2 \quad (2)$$

$$\kappa = P_s t_f / Lw \Delta T_f \quad (3)$$

where P_s and P_r are the heater electrical powers on the sample and reference specimens, respectively. Meanwhile, L and w are the length and width of the heater, respectively.

The micromechanical property measurements that cover the evaluation on hardness and elastic modulus were performed by an ultramicro-indentation measurement system. The indentation system utilizes a continuous stiffness measurement (CSM) method where the measured load and displacement are continuously recorded during the constant indentation process up to a specified maximum load. The system is capable of measuring the hardness without needing to perform in discrete unloading cycles and the constant indentation speed as low as 5 nm/s. The system parameter is ideal to measure a sudden change of micromechanical properties in nonuniform materials because of the existence of certain microstructure defects in the synthesized films [75]. The indenter used is made from diamond, which had almost zero self-deformation due to its high hardness value and the indenter is shaped by Berkovich triangular pyramidal. The hardness value is deduced by the maximum indentation load divided by the projected contact area of the indentation. The projected area is calculated by considering the contact depth, d obtained from the recorded load–displacement curve and an indenter [76].

Meanwhile, the elastic modulus or known as the Young's modulus can be estimated through the measured stiffness of the unloading data recorded after the indentation. An analysis to determine the contact stiffness of the indentation can be computed from a tangent of the upper one-third of unloading curve as proposed by a Doerner–Nix method [77], and the calculation is related with the elastic contact theory [78, 79]. Thus, the sample's Young's modulus, E_s , can be calculated through the following equation,

$$E_s = (1 - \nu_s^2) / \left[(4P/S_l^2\pi)^{1/2} - (1 - \nu_i^2) / E_i \right], \quad (4)$$

where ν_s is the Poisson's ratio of sample, P is the maximum indentation load, and S_l is the slope of the unload curve at the maximum depth point. H is the maximum displacement, both Poisson's ratio, ν_i and Young's modulus, E_i are parameters of the indenter. The values of Poisson's ratio and Young's modulus of the diamond indenter are 0.07 and 1140 GPa, respectively. Meanwhile, the Poisson's ratio of the samples is assumed to be 0.25 as a typical value for most materials especially for the estimation of Young's modulus through indentation test [78, 80].

Acknowledgments

This work was mainly performed in the Micro/Nanomachining Research Education Center (MNC) of Tohoku University and supported by Council for Science, Technology and Innovation (CSTI), Cross-ministerial Strategic Innovation Promotion Program (SIP), Japan (The New Energy and Industrial Technology Development Organization, NEDO). One of the authors, Khairul Fadzli Samat, would like to express his gratitude to Universiti Teknikal Malaysia Melaka (UTeM) and the Ministry of Higher Education Malaysia for supporting this study.

Data availability

The raw/processed data required to reproduce these findings cannot be shared at this time as the data also form part of an ongoing study.

Declarations

Conflict of interest The authors declare that they have no known competing financial interests or personal relationships that could have appeared to influence the work reported in this paper.

References

1. C. GarcíaNúñez, L. Manjakkal, R. Dahiya, Energy autonomous electronic skin. *npj Flex. Electron.* (2019). <https://doi.org/10.1038/s41528-018-0045-x>

2. S. Madakam, R. Ramaswamy, S. Tripathi, Internet of Things (IoT): a literature review. *J. Comput. Commun.* **3**, 164–173 (2015)
3. Y. Chen, N. Chiotellis, L.X. Chuo, C. Pfeiffer, Y. Shi, R.G. Dreslinski, A. Grbic, T. Mudge, D.D. Wentzloff, D. Blaauw, H.S. Kim, Energy-autonomous wireless communication for millimeter-scale internet-of-things sensor nodes. *IEEE J. Sel. Areas Commun.* **34**, 3962–3977 (2016)
4. J. Yan, X. Liao, D. Yan, Y. Chen, Review of micro thermoelectric generator. *J. Microelectromech. Syst.* **27**, 1–18 (2018)
5. C. Gayner, K.K. Kar, Recent advances in thermoelectric materials. *Prog. Mater. Sci.* **83**, 330–382 (2016)
6. W. Liu, K.C. Lukas, K. McEnaney, S. Lee, Q. Zhang, C.P. Opeil, G. Chen, Z. Ren, Studies on the $\text{Bi}_2\text{Te}_3\text{-Bi}_2\text{Se}_3\text{-Bi}_2\text{S}_3$ system for mid-temperature thermoelectric energy conversion. *Energy Environ. Sci.* **6**, 552–560 (2013)
7. T.M. Tritt, Holey and unholly semiconductors. *Science* **283**, 804–805 (1999)
8. F. Yu, J. Zhang, D. Yu, J. He, Z. Liu, B. Xu, Y. Tian, Enhanced thermoelectric figure of merit in nanocrystalline Bi_2Te_3 bulk. *J. Appl. Phys.* **105**, 094303 (2009)
9. A. Zhou, Q. Fu, W. Zhang, B. Yang, J. Li, P. Ziolkowski, E. Mueller, D. Xu, Enhancing the thermoelectric properties of the electroplated Bi_2Te_3 films by tuning the pulse off-to-on ratio. *Electrochim. Acta* **178**, 217–224 (2015)
10. C.V. Manzano, B. Abad, M.M. Rojo, Y.R. Koh, S.L. Hodson, A.M.L. Martinez, X. Xu, A. Shakouri, T.D. Sands, T. Borca-Tasciuc, M. Martin-Gonzalez, Anisotropic effects on the thermoelectric properties of highly oriented electrodeposited Bi_2Te_3 films. *Sci. Rep.* **6**, 19129 (2016)
11. N.H. Trung, N. Van Toan, T. Ono, Fabrication of π -type flexible thermoelectric generators using an electrochemical deposition method for thermal energy harvesting applications at room temperature. *J. Micromech. Microeng. Pap.* **27**, 125006 (2017)
12. N.H. Trung, N. Van Toan, T. Ono, Flexible thermoelectric power generator with Y-type structure using electrochemical deposition process. *Appl. Energy* **1**, 1–10 (2017)
13. Y. Saberi, S.A. Sajjadi, A comprehensive review on the effects of doping process on the thermoelectric properties of Bi_2Te_3 based alloys. *J. Alloys Compd.* **904**, 163918 (2022)
14. F.M. El-Makaty, H.K. Ahmed, K.M. Youssef, The effect of different nanofiller materials on the thermoelectric behavior of bismuth telluride. *Mater. Des.* **209**, 109974 (2021)
15. R. Pandey, P. Thapa, V. Kumar, Y. Zhu, N. Wang, M. Bystrzewski, S.K. Tiwari, Updates in phase change materials for thermoelectric devices: status and challenges. *Materialia* **21**, 101357 (2022)
16. Y. Liu, E. Mu, Z. Wu, Z. Che, F. Sun, X. Fu, F. Wang, X. Wang, Z. Hu, Ultrathin MEMS thermoelectric generator with Bi_2Te_3 /(Pt, Au) multilayers and Sb_2Te_3 legs. *Nano Convergence* **7**(1), 1–11 (2020)
17. T.H. Nguyen, J. Enju, T. Ono, Enhancement of thermoelectric properties of bismuth telluride composite with gold nano-particles inclusions using electrochemical co-deposition. *J. Electrochem. Soc.* **166**, D508–D513 (2019)
18. F.R. Sie, C.H. Kuo, C.S. Hwang, Y.W. Chou, C.H. Yeh, Y.L. Lin, J.Y. Huang, Thermoelectric performance of n-type Bi_2Te_3 /Cu composites fabricated by nanoparticle decoration and spark plasma sintering. *J. Electron. Mater.* **45**, 1927–1934 (2016)
19. Q. Zhang, X. Ai, L. Wang, Y. Chang, W. Luo, W. Jiang, L. Chen, Improved thermoelectric performance of silver nanoparticles-dispersed Bi_2Te_3 composites deriving from hierarchical two-phased heterostructure. *Adv. Funct. Mater.* **25**, 966–976 (2015)
20. H. Huang, P. Wen, T. Bi, B. Duan, X. Zhou, Y. Li, P. Zhai, Influence of graphene oxide nanosheets and multi-walled carbon nanotubes on the thermoelectric and mechanical properties of $\text{Mg}_2(\text{Si}_{0.3}\text{Sn}_{0.7})_{0.99}\text{Sb}_{0.01}$. *Scr. Mater.* **203**, 114103 (2021)
21. A. Nag, M.E.E. Alahi, S.C. Mukhopadhyay, Recent progress in the fabrication of graphene fibers and their composites for applications of monitoring human activities. *Appl. Mater. Today* **22**, 100953 (2021)
22. Y. Du, S.Z. Shen, K. Cai, P.S. Casey, Research progress on polymer-inorganic thermoelectric nanocomposite materials. *Prog. Polym. Sci.* **37**, 820–841 (2012)
23. K.T. Kim, S.Y. Choi, E.H. Shin, K.S. Moon, H.Y. Koo, G.G. Lee, G.H. Ha, The influence of CNTs on the thermoelectric properties of a CNT/ Bi_2Te_3 composite. *Carbon* **52**, 541–549 (2013)
24. S. Kumar, D. Chaudhary, P. Kumar Dhawan, R.R. Yadav, N. Khare, Bi_2Te_3 -MWCNT nanocomposite: an efficient thermoelectric material. *Ceram. Int.* **43**, 14976–14982 (2017)
25. Y. Zhang, X.L. Wang, W.K. Yeoh, R.K. Zeng, C. Zhang, Electrical and thermoelectric properties of single-wall carbon nanotube doped Bi_2Te_3 . *Appl. Phys. Lett.* **101**, 031909 (2012)
26. H. An, D. Karas, B.W. Kim, S. Trabia, J. Moon, Flexible n-type thermoelectric composite films with enhanced performance through interface engineering and post-treatment. *Nanotechnology* **29**, 275403 (2018)
27. K. Ahmad, C. Wan, Enhanced thermoelectric performance of Bi_2Te_3 through uniform dispersion of single wall carbon nanotubes. *Nanotechnology* **28**, 415402 (2017)
28. K.F. Samat, N.H. Trung, T. Ono, Enhancement in thermoelectric performance of electrochemically deposited platinum-bismuth telluride nanocomposite. *Electrochim. Acta* **312**, 62–71 (2019)
29. D.K. Ko, Y. Kang, C.B. Murray, Enhanced thermopower via carrier energy filtering in solution-processable Pt- Sb_2Te_3 nanocomposites. *Nano Lett.* **11**, 2841–2844 (2011)
30. W.L. Wang, C.C. Wan, Y.Y. Wang, Composition-dependent characterization and optimal control of electrodeposited Bi_2Te_3 films for thermoelectric application. *Electrochim. Acta* **52**, 6502–6508 (2007)
31. Y. Ma, E. Ahlberg, Y. Sun, B.B. Iversen, A.E.C. Palmqvist, Thermoelectric properties of thin films of bismuth telluride

- electrochemically deposited on stainless steel substrates. *Electrochim. Acta* **56**, 4216–4223 (2011)
32. W.S. Kang, W.J. Li, W.C. Chou, M.F. Tseng, C.S. Lin, Microstructure and thermoelectric properties of Bi_2Te_3 electrodeposits plated in nitric and hydrochloric acid baths. *Thin Solid Films* **623**, 90–97 (2017)
 33. J.R. Roos, J.P. Celis, J. Franssaer, C. Buelens, The development of composite plating for advanced materials. *JOM* **42**, 60–63 (1990)
 34. C.T.J. Low, R.G.A. Wills, F.C. Walsh, Electrodeposition of composite coatings containing nanoparticles in a metal deposit. *Surf. Coat. Technol.* **201**, 371–383 (2006)
 35. P.M. Vereecken, I. Shao, P.C. Searson, Particle codeposition in nanocomposite films. *J. Electrochem. Soc.* **147**(7), 2572–2575 (2000)
 36. P. Berçot, E. Pea-Muoz, J. Pagetti, Electrolytic composite Ni-PTFE coatings: an adaptation of Guglielmi's model for the phenomena of incorporation. *Surf. Coat. Technol.* **157**, 282–289 (2002)
 37. M.M. Rashid, K.H. Cho, G.-S. Chung, Rapid thermal annealing effects on the microstructure and the thermoelectric properties of electrodeposited Bi_2Te_3 film. *Appl. Surf. Sci.* **279**, 23–30 (2013)
 38. P.B. Patil, S.S. Mali, V.V. Kondalkar, R.M. Mane, P.S. Patil, C.K. Hong, P.N. Bhosale, Morphologically controlled electrodeposition of fern shaped Bi_2Te_3 thin films for photoelectrochemical performance. *J. Electroanal. Chem.* **758**, 178–190 (2015)
 39. J. Na, Y. Kim, T. Park, C. Park, E. Kim, Preparation of bismuth telluride films with high thermoelectric power factor. *ACS Appl. Mater. Interfaces* **8**, 32392–32400 (2016)
 40. Y. Yoon, G.S. Lee, K. Yoo, J.B. Lee, Fabrication of a microneedle/CNT hierarchical micro/nano surface electrochemical sensor and its In-vitro glucose sensing characterization. *Sensor* **13**, 16672–16681 (2013)
 41. N.V. Long, C.M. Thi, M. Nogami, M. Ohtaki, Novel issues of morphology, size, and structure of Pt nanoparticles in chemical engineering: surface attachment, aggregation or agglomeration, assembly, and structural changes. *New J. Chem.* **36**, 1320 (2012)
 42. L. Yin, L. Sun, P. Jiang, X. Bao, Achieving p-type conductivity in $\text{ZnO}/\text{Bi}_{0.5}\text{Sb}_{1.5}\text{Te}_3$ composites. *J. Energy Chem.* **53**, 163–167 (2020)
 43. S.V. Faleev, F. Léonard, Theory of enhancement of thermoelectric properties of materials with nanoinclusions. *Phys. Rev. B* **77**, 1–9 (2008)
 44. R.L.F.M. Cutler, J.F. Leavy, Electronic transport in semimetallic cerium sulfide. *Phys. Rev.* (1964). <https://doi.org/10.1103/PhysRev.133.A1143>
 45. C. Kittel, P. McEuen, P. McEuen, *Introduction to Solid State Physics*, 8th edn. (Wiley, New York, 1996)
 46. G. Chen, *Nanoscale Energy Transport and Conversion: A Parallel Treatment of Electrons, Molecules, Phonons, and Photons* (Oxford University Press, Oxford, 2005)
 47. W. Kim, Strategies for engineering phonon transport in thermoelectrics. *J. Mater. Chem. C* **3**, 10336–10347 (2015)
 48. L.D. Hicks, M.S. Dresselhaus, Thermoelectric figure of merit of a one-dimensional conductor. *Phys. Rev. B* **47**(24), 16631 (1993)
 49. T. Sun, M.K. Samani, N. Khosravian, K.M. Ang, Q. Yan, B.K. Tay, H.H. Hng, Enhanced thermoelectric properties of n-type $\text{Bi}_2\text{Te}_{2.7}\text{Se}_{0.3}$ thin films through the introduction of Pt nanoinclusions by pulsed laser deposition. *Nano Energy* **8**, 223–230 (2014)
 50. L.D. Zhao, B.P. Zhang, W.S. Liu, J.F. Li, Effect of mixed grain sizes on thermoelectric performance of Bi_2Te_3 compound. *J. Appl. Phys.* **105**, 023704 (2009)
 51. D.H. Kim, T. Mitani, Thermoelectric properties of fine-grained Bi_2Te_3 alloys. *J. Alloys Compd.* **399**, 14–19 (2005)
 52. S. Spanou, E.A. Pavlatou, N. Spyrellis, Ni/nano-TiO₂ composite electrodeposits: textural and structural modifications. *Electrochim. Acta* **54**, 2547–2555 (2009)
 53. H. Gleiter, Grain boundaries as point defect sources or sinks—diffusional creep. *Acta Metall.* **27**, 187–192 (1979)
 54. P. Chakraborty, L. Cao, Y. Wang, Ultralow lattice thermal conductivity of the random multilayer structure with lattice imperfections. *Sci. Rep.* **7**, 1–8 (2017)
 55. Y. Song, I.J. Yoo, N.R. Heo, D.C. Lim, D. Lee, J.Y. Lee, K.H. Lee, K.H. Kim, J.H. Lim, Electrodeposition of thermoelectric Bi_2Te_3 thin films with added surfactant. *Curr. Appl. Phys.* **15**, 261–264 (2015)
 56. L. Sun, G.L. Warren, J.Y. O'reilly, W.N. Everett, S.M. Lee, D. Davis, D. Lagoudas, H.J. Sue, Mechanical properties of surface-functionalized SWCNT/epoxy composites. *Carbon* **46**, 320–328 (2008)
 57. M.F. Yu, B.S. Files, S. Arepalli, R.S. Ruoff, Tensile loading of ropes of single wall carbon nanotubes and their mechanical properties. *Phys. Rev. Lett.* **84**, 5552–5555 (2000)
 58. A. Allaoui, S. Bai, H.M. Cheng, J.B. Bai, Mechanical and electrical properties of a MWNT/epoxy composite. *Compos. Sci. Technol.* **62**, 1993–1998 (2002)
 59. V.V. Mokashi, D. Qian, Y. Liu, A study on the tensile response and fracture in carbon nanotube-based composites using molecular mechanics. *Compos. Sci. Technol.* **67**, 530–540 (2007)
 60. K. Liao, S. Li, Interfacial characteristics of a carbon nanotube-polystyrene composite system. *Appl. Phys. Lett.* **79**, 4225–4227 (2001)
 61. T. Fujigaya, N. Nakashima, Non-covalent polymer wrapping of carbon nanotubes and the role of wrapped polymers as functional dispersants. *Sci. Technol. Adv. Mater.* **16**, 024802 (2015)
 62. S. Ramesh, L.M. Ericson, V.A. Davis, R.K. Saini, C. Kittrell, M. Pasquali, W.E. Billups, W.W. Adams, R.H. Hauge, R.E. Smalley, Dissolution of pristine single walled carbon nanotubes in superacids by direct protonation. *J. Phys. Chem. B* **108**, 8794–8798 (2004)
 63. N. Nakashima, Soluble carbon nanotubes: fundamentals and applications. *Int. J. Nanosci.* **4**, 119–137 (2005)
 64. P.K. Rai, R.A. Pinnick, A.N.G. Parra-Vasquez, V.A. Davis, H.K. Schmidt, R.H. Hauge, R.E. Smalley, M. Pasquali,

- Isotropic–nematic phase transition of single-walled carbon nanotubes in strong acids. *J. Am. Chem. Soc.* **128**, 591–595 (2006)
65. D. Tasis, N. Tagmatarchis, A. Bianco, M. Prato, Chemistry of carbon nanotubes. *Chem. Rev.* **106**, 1105–1136 (2006)
 66. D.Q. Yang, J.F. Rochette, E. Sacher, Spectroscopic evidence for π - π interaction between poly (diallyl dimethylammonium) chloride and multiwalled carbon nanotubes. *J. Phys. Chem. B* **109**, 4481–4484 (2005)
 67. J. Shi, Steric stabilization, in *Croup Inorganic Materials Science-Literature Review*. (Ohio State University, Columbus, 2002)
 68. Y. Min, M. Akbulut, K. Kristiansen, Y. Golan, J. Israelachvili, The role of interparticle and external forces. *Nat. Mater.* **7**, 527–538 (2008)
 69. G. Testa, L. Fontana, I. Venditti, I. Fratoddi, Functionalized platinum nanoparticles with surface charge triggered by pH: synthesis, characterization and stability studies. *Beilstein J. Nanotechnol.* **7**, 1822–1828 (2016)
 70. D. Landolt, A. Marlot, Microstructure and composition of pulse-plated metals and alloys. *Surf. Coat. Technol.* **169–170**, 8–13 (2003)
 71. M.S. Chandrasekar, M. Pushpavanam, Pulse and pulse reverse plating-conceptual, advantages and applications. *Electrochim. Acta* **53**, 3313–3322 (2008)
 72. N. Trung, K. Sakamoto, N. Toan, T. Ono, Synthesis and evaluation of thick films of electrochemically deposited Bi_2Te_3 and Sb_2Te_3 thermoelectric materials. *Materials* **10**, 154 (2017)
 73. ASTM Standard F76, in *Standard Test Methods for Measuring Resistivity and Hall Coefficient and Determining Hall Mobility in Single-Crystal Semiconductors* (ASTM International, West Conshohocken, 2008). <https://doi.org/10.1520/F0076-08>
 74. A. Zhou, W. Wang, B. Yang, J. Li, Q. Zhao, Thermal conductivity study of micrometer-thick thermoelectric films by using three-omega methods. *Appl. Therm. Eng.* **98**, 683–689 (2016)
 75. X. Li, B. Bhushan, A review of nanoindentation continuous stiffness measurement technique and its applications. *Mater. Charact.* **48**, 11–36 (2002)
 76. Y. Tsukamoto, H. Yamaguchi, M. Yanagisawa, Mechanical properties of thin films: measurements of ultramicroindentation hardness, Young's modulus and internal stress. *Thin Solid Films* **154**, 1987 (1987)
 77. M.F. Doerner, D.S. Gardner, W.D. Nix, Plastic properties of thin films on substrates as measured by submicron indentation hardness and substrate curvature techniques. *J. Mater. Res.* **1**, 845–851 (1986)
 78. ASM International, Handbook Committee, *ASM Handbook: Mechanical Testing and Evaluation*, vol. 8 (ASM International, Materials Park, 2000)
 79. W.C. Oliver, G.M. Pharr, Measurement of hardness and elastic modulus by instrumented indentation: advances in understanding and refinements to methodology. *J. Mater. Res.* **19**, 3–20 (2004)
 80. J.E. Zorzi, C.A. Perottoni, Estimating Young's modulus and Poisson's ratio by instrumented indentation test. *Mater. Sci. Eng. A* **574**, 25–30 (2013)
- Springer Nature or its licensor holds exclusive rights to this article under a publishing agreement with the author(s) or other rightsholder(s); author self-archiving of the accepted manuscript version of this article is solely governed by the terms of such publishing agreement and applicable law.